# A Hybrid Method for the Efficient Calculation of the Band Structure of 3-D Metallic Crystals

Mário G. Silveirinha, *Member, IEEE,* and Carlos A. Fernandes, *Member, IEEE*

***Abstract*—In this paper, we propose a new hybrid method to characterize the band structure of three-dimensional metallic crystals. We formulate an auxiliary problem that has the same spectrum as the metallic crystal. We prove that the spectrum of the auxiliary problem can be efficiently computed using the plane-wave method and the method of moments. Thus, the band structure of the metallic crystal can also be efficiently calculated. Our approach is much more effective than root-searching methods, because all of the eigenvalues are obtained at once and degenerate cases pose no difficulty. This is a generalization of a previously proposed method for two-dimensional structures.**

***Index Terms*—Electromagnetic bandgap materials, homogenization theory, metamaterials, photonic crystals.**

## I. Introduction

In RECENT years, the propagation of electromagnetic waves in periodic dielectric/metallic structures has received great attention [1]. A variety of potential applications to many scientific areas and engineering have been suggested. Examples include inhibition of spontaneous emission in semiconductor lasers [2], high-impedance surfaces [3], exotic materials with negative permittivity and permeability [4], improvement of the radiation characteristic of antennas [5], and synthesis of waveguide filters [6].

The analysis of periodic structures is thus a problem of increasing importance. However, it is in general a difficult problem because it involves the analysis of electrically large complex structures, which is computationally demanding. The calculation of the band structure of a periodic medium is no exception. The problem involves the calculation of the eigenvalues of a differential operator. Several methods have been developed for the effect, e.g., the plane-wave method [1], the order-$N$ method [7], and the transfer matrix method (TMM) [8].

Recently [9], [10], the authors of this paper proposed a new hybrid plane-wave-integral-equation-based method to compute the band structure of periodic media with cylindrical inclusions (two-dimensional (2-D) problem). In this paper, we generalize the method to the three-dimensional (3-D) case.

Manuscript received May 28, 2003; revised October 16, 2003. This work was supported by the Fundação para Ciência e a Tecnologia under Project POSI 34860/99.

M. G. Silveirinha is with the Electrical Engineering Department, Polo II da Universidade de Coimbra, 3030 Coimbra, Portugal (e-mail: mario.silveirinha@co.it.pt).

C. A. Fernandes is with the Instituto Superior Técnico, Technical University of Lisbon, 1049-001 Lisbon, Portugal (e-mail: carlos.fernandes@lx.it.pt).

Digital Object Identifier 10.1109/TMTT.2004.823563

As discussed in detail in [11] and [12], the discontinuities of the electric permittivity at the dielectric interfaces cause the standard plane wave to converge slowly. Indeed, the plane-wave expansions of the pertinent physical quantities fluctuate intensely around the dielectric interfaces in a manifestation of the well-known Gibbs phenomenon. Consequently, a very large number of plane waves may be required for the accurate computation of the band structure of a dielectric crystal. In some cases, the computational resources may be insufficient to reach convergence [12], [13]. In the nondispersive metallic case, in which the inclusions are perfect electric conductors (PECs), the situation is particularly acute. Indeed, this case can be regarded as the limit situation of a dielectric crystal with infinite dielectric contrast. This configuration precludes the convergence of the standard plane-wave method, which is not applicable in the metallic case. To circumvent this situation, the authors of this paper proposed in [9] a regularization procedure for the eigenfunctions of the metallic crystal. The regularization procedure is also partially related with the boundary integral resonant method utilized in [14] and [15] to determine the resonant modes of metallic waveguides and cavities. We proposed an auxiliary integral-differential problem with the same band structure as the metallic crystal. It was proven that the eigenfunctions of the auxiliary problem are much smoother than the electromagnetic modes of the metallic crystal, and thus that the plane-wave method was suitable to compute the band structure of the auxiliary problem (which is coincident with that of the metallic crystal) very efficiently. The analysis of [9], however, is limited to the 2-D case in which the inclusions are metallic cylinders with arbitrary cross section. In this paper, we extend the proposed formalism to compute the band structure of 3-D metallic crystals. The generalization is far from trivial since the vector nature of radiation introduces considerable difficulties. Indeed, apart from the philosophy of the method that seeks to improve the regularity of the electromagnetic fields using layer potentials, the formulation and results are significantly different. The formulation for the dielectric case will be presented elsewhere [10].

The outline of this paper is as follows. In Section II, we present the formulation and describe the geometry of the problem. In Section III, we prove that the band structure of the metallic crystal is coincident with that of an auxiliary integral-differential eigensystem. In Section IV, we explain how the integral-differential is discretized numerically using the plane-wave method and the method of moments (MoM) and how the spectrum of the metallic crystal can be efficiently computed numerically. In Section V, we present several numerical examples that illustrate the application of the method, and in Section VI we draw the conclusions.

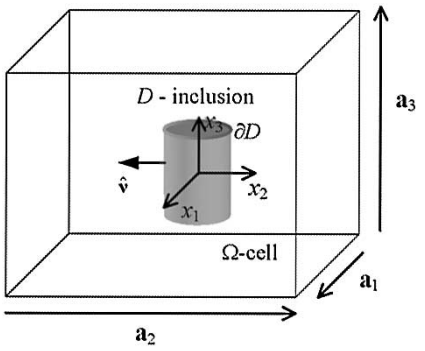


Fig. 1. Geometry of the unit cell associated with the metallic inclusion $D$.

## II. Formulation

We study the propagation of electromagnetic waves in metallic media with arbitrary inclusion shapes. The artificial medium consists of a 3-D periodic array of PEC metallic inclusions embedded into a host dielectric material. We assume without loss of generality that the host medium is air.

The lattice primitive vectors are $\mathbf{a}_1, \mathbf{a}_2$, and $\mathbf{a}_3$. The unit cell $\Omega$ is depicted in Fig. 1 for the case of the primitive vectors being orthogonal. The metallic region in the unit cell is $D$ and the boundary of $D$ is the surface $\partial D$. The outward unit vector normal to $\partial D$ is $\hat{\boldsymbol{\nu}}$. The translation of $\partial D$ into the lattice point $\mathbf{r_I} = i_1\mathbf{a}_1 + i_2\mathbf{a}_2 + i_3\mathbf{a}_3$ is $\partial D_{\mathbf{I}}$, where $\mathbf{I} = (i_1, i_2, i_3)$ is a multi-index of integers.

The objective is to characterize the electromagnetic Floquet modes of the metallic crystal. A generic mode $(\mathbf{E}, \mathbf{H})$ satisfies the following:

$$\nabla \times \mathbf{E} = -j\beta Z_0 \mathbf{H}, \qquad \mathbf{r} \notin \partial D_{\mathbf{I}} \tag{1a}$$

$$\nabla \times \mathbf{H} = j\frac{\beta}{Z_0}\mathbf{E}, \qquad \mathbf{r} \notin \partial D_{\mathbf{I}} \tag{1b}$$

$$\hat{\boldsymbol{\nu}} \times \mathbf{E} = \mathbf{0}, \qquad \text{on } \partial D_{\mathbf{I}} \tag{1c}$$

$$(\mathbf{E}, \mathbf{H}) \exp(j\mathbf{k}\cdot\mathbf{r}) \text{ is periodic} \tag{1d}$$

where $\mathbf{k} = (k_1, k_2, k_3)$ is the wave vector, $Z_0$ is the impedance of the host medium, $\beta = \omega/c$ is the free-space wavenumber, $\omega$ is the angular frequency, and $c$ is the velocity of light in vacuum. Equations (1a) and (1b) are the frequency-dependent Maxwell's equations, (1c) is the boundary condition at the metallic interfaces, and (1d) is the Floquet wave condition.

For a given wave vector $\mathbf{k}$, system (1) has nontrivial solutions for a countable set of resonant wavenumbers. The resonant wavenumbers $\beta_n = \beta_n(\mathbf{k})$, $n = 1, 2, \ldots$, form the band structure of the metallic crystal. In this paper, we generalize the hybrid method proposed in [9] to the 3-D case, and we compute the band structure of several relevant metallic crystals.

To begin with, it is important to discuss some properties of the Floquet eigenfunctions that satisfy (1). The eigenfunctions of system (1) are assumed to be defined in all space. Indeed, the mathematical formulation inherently assumes that the inclusions are hollow. From the physical point-of-view, this is irrelevant, since a perfect conductor completely isolates the interior and exterior of the inclusions. The tangential component of the electric field vanishes at both sides of the metallic interfaces. The electromagnetic modes relevant to describe propagation in the metallic crystal are such that $(\mathbf{E}, \mathbf{H}) = (\mathbf{0}, \mathbf{0})$ inside the PEC inclusions (external solutions). Indeed, the propagation of electromagnetic waves in the metallic crystal is mathematically an *exterior problem*.

The eigensystem (1) has solutions that are not external. It is easy to prove that the solutions of (1) can be written as a direct sum of external modes and internal modes. The external modes vanish inside the inclusions and correspond to the Floquet modes of the metallic crystal. On the other hand, the internal modes vanish outside the inclusions and correspond to the electromagnetic modes of a metallic cavity with the same shape as a generic inclusion. The internal modes must be removed from the spectrum of (1).

The internal modes can be easily detected since the associated bands are flat (dispersionless, i.e., independent of the wave vector). Alternatively, we can recognize if a given eigenvalue of (1) is associated with an internal mode by testing if the corresponding eigenfunction verifies $(\mathbf{E}, \mathbf{H}) \neq (\mathbf{0}, \mathbf{0})$ inside the metallic inclusions. Since the discussion is analogous to that of [9], we omit further details here. We merely point out that, in the important case in which the metallic inclusions can be considered infinitesimally thin (e.g., planar inclusions), there are no internal modes. In that situation, the band structure of (1) coincides exactly with the spectrum of the metallic crystal.

## III. Integral-Differential Eigensystem

In this section, we introduce an auxiliary integral-differential eigensystem that is equivalent to the eigensystem (1) (i.e., both systems have the same band structure). The important difference between the two problems relates to the regularity of the respective eigenfunctions. Indeed, the normal component of the electric field and the tangential component of the magnetic field have jump discontinuities at the metallic interfaces and, thus, the electromagnetic modes of the metallic crystal are discontinuous. In contrast, the solutions of the auxiliary eigensystem are smooth functions. In Section IV, we explain how to take advantage of this fact to compute very efficiently the band structure of metallic crystals. The proof of the results enunciated in this section was moved to Appendix B to ease the readability of the paper.

The integral-differential eigensystem is defined by the following set of coupled equations:

$$\nabla^2\tilde{\mathbf{E}} + \beta^2 \left( \tilde{\mathbf{E}}(\mathbf{r}) - \int_{\partial D} \mathbf{f}(\mathbf{r}')\Phi_p(\mathbf{r}\,|\,\mathbf{r}')\,ds' + \nabla \int_{\partial D} \nabla'_S \cdot \mathbf{f}\, G_1(\mathbf{r}\,|\,\mathbf{r}')\,ds' \right) = 0 \tag{2a}$$

$$\nabla \cdot \tilde{\mathbf{E}} = 0 \tag{2b}$$

$$-\int_{\partial D} \mathbf{w}^*(\mathbf{r})\tilde{\mathbf{E}}\cdot(\mathbf{r})\,ds + \int_{\partial D}\int_{\partial D} \mathbf{w}^*(\mathbf{r})\cdot\mathbf{f}(\mathbf{r}')\,\Phi_p(\mathbf{r}\,|\,\mathbf{r}')ds'ds + \int_{\partial D}\int_{\partial D} \nabla_S\cdot\mathbf{w}^*\nabla'_S\cdot\mathbf{f}\,G_1(\mathbf{r}\,|\,\mathbf{r}')\,ds'ds = \frac{1}{\beta^2}\int_{\partial D}\int_{\partial D} \nabla_S\cdot\mathbf{w}^*\nabla'_S\cdot\mathbf{f}\,\Phi_p(\mathbf{r}\,|\,\mathbf{r}')\,ds'ds \tag{2c}$$

$$\tilde{\mathbf{E}}\exp(j\,\mathbf{k}\cdot\mathbf{r}) \text{ is periodic.} \tag{2d}$$

A generic eigenfunction is represented by the pair $(\tilde{\mathbf{E}}, \mathbf{f})$, where $\tilde{\mathbf{E}}$ is a Floquet vector field defined over all space and $\mathbf{f}$ is a tangential vector density defined over surface $\partial D$ (ahead we shall see that $\mathbf{f}$ can be related with a current density). Equation (2c) must hold for an arbitrary tangential density $\mathbf{w} = \mathbf{w}(\mathbf{r})$ defined over $\partial D$. In (2), the symbol "*" stands for complex conjugation, and $\nabla_S \cdot$ represents the surface divergence of a tangential vector field.

The potentials $\Phi_p(\mathbf{r} \,|\, \mathbf{r}')$ and $G_1(\mathbf{r} \,|\, \mathbf{r}')$ are the pseudoperiodic Green's functions introduced next. As usual, the primed coordinates $\mathbf{r}' = (x_1', x_2', x_3')$ refer to a generic source point. The potential $\Phi_p$ is the Floquet solution of the following equation:

$$\nabla^2 \Phi_p = -e^{-j\mathbf{k}\cdot(\mathbf{r}-\mathbf{r}')} \sum_{\mathbf{I}} \delta(\mathbf{r} - \mathbf{r}' - \mathbf{r}_\mathbf{I}) \tag{3}$$

where $\mathbf{I} = (i_1, i_2, i_3)$ is a multi-index of integers, and $\mathbf{r}_\mathbf{I} = i_1\mathbf{a}_1 + i_2\mathbf{a}_2 + i_3\mathbf{a}_3$ is generic lattice point. We refer to $\Phi_p$ as the lattice Green's function [16]–[18]. On the other hand, the Green's function $G_1$ is the Floquet solution of

$$\nabla^2 G_1 = \Phi_p(\mathbf{r} \,|\, \mathbf{r}'). \tag{4}$$

Both Green's functions are Floquet potentials with wave vector $\mathbf{k}$. The Green's functions can be efficiently evaluated using the formulas presented in Appendix A.

For a given wave vector $\mathbf{k}$, (2) is a homogeneous problem and thus has nontrivial solutions $(\tilde{\mathbf{E}}, \mathbf{f})$ only for specific resonant wavenumbers $\beta = \beta_n(\mathbf{k})$, $n = 1, 2, \ldots,$ As proven in Appendix B, the vector field $\tilde{\mathbf{E}}$ is smooth everywhere since it has continuous derivatives up to order two in all space, including on the metallic interfaces. We also prove in Appendix B that the eigenvalues of (2) are coincident with those of system (1). Indeed, there is a one-to-one mapping between the eigenfunctions of (1) (represented by the vector field $\mathbf{E}$) and the eigenfunctions of (2) (represented by the pair $(\tilde{\mathbf{E}}, \mathbf{f})$). The mapping $\mathbf{E} \to (\tilde{\mathbf{E}}, \mathbf{f})$ is defined by the following equations:

$$\mathbf{f} = j\,\beta\, Z_0 \hat{\boldsymbol{\nu}} \times [\mathbf{H}], \qquad \mathbf{r} \in \partial D \tag{5}$$

$$\begin{aligned} \tilde{\mathbf{E}}(\mathbf{r}) = \mathbf{E}(\mathbf{r}) &+ \int_{\partial D} \mathbf{f}(\mathbf{r}')\, \Phi_p(\mathbf{r} \,|\, \mathbf{r}')\, ds' \\ &- \nabla \int_{\partial D} \nabla'_S \cdot \mathbf{f}\; G_1(\mathbf{r} \,|\, \mathbf{r}')\, ds' \\ &+ \frac{1}{\beta^2} \nabla \int_{\partial D} \nabla'_S \cdot \mathbf{f}\, \Phi_p(\mathbf{r} \,|\, \mathbf{r}')\, ds'. \end{aligned} \tag{6}$$

In the above, $[\mathbf{H}] = \mathbf{H}_+ - \mathbf{H}_-$, where $\mathbf{H}_+$ and $\mathbf{H}_-$ refer to the magnetic field $\mathbf{H}$ calculated from the outer side and from the inner side of $\partial D$, respectively. Thus, the tangential vector $\mathbf{f}$ is proportional to the electric current over the metallic surface $\partial D$. The inverse mapping $(\tilde{\mathbf{E}}, \mathbf{f}) \to \mathbf{E}$ is obtained from (6) by rearranging the terms.

## IV. Numerical Solution of the Integral-Differential Eigensystem

In the following, we discretize the integral-differential eigensystem (2) and explain how it can be solved numerically.

### A. Discretization of the Eigensystem

The objective of this section is to reduce (2) into the matrix form. Since the auxiliary field $\tilde{\mathbf{E}}$ is a smooth vector field with continuous derivatives up to order 2 in all space, it is appropriate to expand it into a fast converging plane-wave series. From (2b), the vector field is transverse, and thus it can be expanded into transverse plane waves as follows:

$$\tilde{\mathbf{E}}(\mathbf{r}) = \sum_{\mathbf{J}} \sum_{s=1,2} c_\mathbf{J}^s \mathbf{e}_\mathbf{J}^s(\mathbf{r}) \tag{7}$$

where $\mathbf{J} = (j_1, j_2, j_3)$ is an arbitrary multi-index of integers that identifies the wave vector of the plane wave, $s = 1, 2$ identifies the polarization of the plane wave, $c_\mathbf{J}^1$ and $c_\mathbf{J}^2$ are the unknown coefficients of the plane-wave expansion, and the fields $\mathbf{e}_\mathbf{J}^1(\mathbf{r})$ and $\mathbf{e}_\mathbf{J}^2(\mathbf{r})$ are defined by

$$\mathbf{e}_\mathbf{J}^s(\mathbf{r}) = g_\mathbf{J}(\mathbf{r})\, \mathbf{p}_\mathbf{J}^s, \qquad s = 1, 2 \tag{8a}$$

$$\mathbf{k}_\mathbf{J} \cdot \mathbf{p}_\mathbf{J}^1 = \mathbf{k}_\mathbf{J} \cdot \mathbf{p}_\mathbf{J}^2 = 0$$

$$\mathbf{p}_\mathbf{J}^r \cdot \mathbf{p}_\mathbf{J}^s = \delta_{r,s}, \qquad r, s = 1, 2 \tag{8b}$$

where $\mathbf{p}_\mathbf{J}^1$ and $\mathbf{p}_\mathbf{J}^2$ are real vectors that define the polarization of $\tilde{\mathbf{E}}$, and $g_\mathbf{J}$ is the plane wave as follows:

$$g_\mathbf{J}(\mathbf{r}) = \frac{1}{\sqrt{V_{\text{cell}}}} e^{-j\mathbf{k}_\mathbf{J}\cdot\mathbf{r}}, \qquad \mathbf{k}_\mathbf{J} = \mathbf{k} + j_1\mathbf{b}_1 + j_2\mathbf{b}_2 + j_3\mathbf{b}_3 \tag{9}$$

where $V_{\text{cell}} = |\mathbf{a}_1 \cdot \mathbf{a}_2 \times \mathbf{a}_3|$ denotes the volume of the unit cell and $\mathbf{b}_1, \mathbf{b}_2$, and $\mathbf{b}_3$ are the primitive vectors of the reciprocal lattice defined by $\mathbf{a}_n \cdot \mathbf{b}_m = 2\pi\, \delta_{n,m}, m, n = 1, 2, 3$ [1], where $\delta_{n,m} = 1$ if $n = m$ and $\delta_{n,m} = 0$ otherwise.

For convenience, we define the following scalar product over the unit cell:

$$\langle \mathbf{F}_1 \,|\, \mathbf{F}_2 \rangle = \int_\Omega \mathbf{F}_1^*(\mathbf{r}) \cdot \mathbf{F}_2(\mathbf{r})\, d^3\mathbf{r} \tag{10}$$

where $\mathbf{F}_1$ and $\mathbf{F}_2$ stand for generic vector fields.

We substitute (7) into (2a) and calculate the scalar product of both sides of the resulting equation with the generic plane wave $\mathbf{e}_\mathbf{I}^r$. Since plane waves with different indexes are orthonormal, we obtain

$$\begin{aligned} -|\mathbf{k}_\mathbf{I}|^2 c_\mathbf{I}^r + \beta^2 \Bigg( c_\mathbf{I}^r &- \int_{\partial D} \langle \mathbf{e}_\mathbf{I}^r(\mathbf{r}) |\, \mathbf{f}(\mathbf{r}') \Phi_p(\mathbf{r} \,|\, \mathbf{r}') \rangle\, ds' \\ &+ \int_{\partial D} \nabla'_S \cdot \mathbf{f}\, \langle \mathbf{e}_\mathbf{I}^r(\mathbf{r}) |\, \nabla G_1(\mathbf{r} \,|\, \mathbf{r}') \rangle\, ds' \Bigg) = 0. \end{aligned} \tag{11}$$

Integrating by parts and using the fact that $\mathbf{e}_{\mathbf{I}}^r$ and $G_1$ are Floquet waves associated with the wave vector $\mathbf{k}$, we find

$$\begin{aligned}\left\langle \mathbf{e}_{\mathbf{I}}^r(\mathbf{r})\middle|\nabla G_1(\mathbf{r}\,|\,\mathbf{r}')\right\rangle &= \int_\Omega \left(\mathbf{e}_{\mathbf{I}}^r(\mathbf{r})\right)^*\cdot\nabla G_1(\mathbf{r}\,|\,\mathbf{r}')d^3\mathbf{r}\\ &= -\int_\Omega \left(\nabla\cdot\mathbf{e}_{\mathbf{I}}^r(\mathbf{r})\right)^* G_1(\mathbf{r}\,|\,\mathbf{r}')d^3\mathbf{r}\\ &= 0. \end{aligned} \tag{12}$$

The rightmost identity is a consequence of the plane wave being transverse, i.e., $\nabla\cdot\mathbf{e}_{\mathbf{I}}^r(\mathbf{r})=0$.

On the other hand, from the spectral representation of the lattice Green's function (A1), we obtain

$$\begin{aligned}\left\langle \mathbf{e}_{\mathbf{I}}^r(\mathbf{r})\middle|\,\mathbf{f}(\mathbf{r}')\Phi_p(\mathbf{r}\,|\,\mathbf{r}')\right\rangle &= \mathbf{p}_{\mathbf{I}}^r\cdot\mathbf{f}(\mathbf{r}')\int_\Omega g_{\mathbf{I}}^*(\mathbf{r})\Phi_p(\mathbf{r}\,|\,\mathbf{r}')d^3\mathbf{r}\\ &= \mathbf{p}_{\mathbf{I}}^r\cdot\mathbf{f}(\mathbf{r}')\frac{1}{|\mathbf{k}_{\mathbf{I}}|^2}g_{\mathbf{I}}^*(\mathbf{r}'). \end{aligned} \tag{13}$$

Thus, (11) simplifies to

$$|\mathbf{k}_{\mathbf{I}}|^2 c_{\mathbf{I}}^r - \int_{\partial D}\left(\mathbf{e}_{\mathbf{I}}^r(\mathbf{r}')\right)^*\cdot\mathbf{f}(\mathbf{r}')ds' = \frac{|\mathbf{k}_{\mathbf{I}}|^4}{\beta^2}c_{\mathbf{I}}^r. \tag{14}$$

To keep the notation short, we define the following scalar product over $\partial D$:

$$\langle\mathbf{h}_1\,|\,\mathbf{h}_2\rangle_{\partial D} = \int_{\partial D}\left(\mathbf{h}_1(\mathbf{r})\right)^*\cdot\mathbf{h}_2(\mathbf{r})\,ds \tag{15}$$

where $\mathbf{h}_1$ and $\mathbf{h}_2$ are generic vector fields. Using this definition, we can rewrite (14) as

$$|\mathbf{k}_{\mathbf{I}}|^2 c_{\mathbf{I}}^r - \langle\mathbf{e}_{\mathbf{I}}^r|\,\mathbf{f}\rangle_{\partial D} = \frac{|\mathbf{k}_{\mathbf{I}}|^4}{\beta^2}c_{\mathbf{I}}^r, \qquad \mathbf{I}\text{ arbitrary};\quad r=1,2. \tag{16}$$

The above concludes the discretization of (2a).

Next, we discretize (2c) using the MoM. To this end, we expand the tangential density $\mathbf{f}$ as follows:

$$\mathbf{f}(\mathbf{r}') = \sum_n d_n\mathbf{f}_n(\mathbf{r}') \tag{17}$$

where $\mathbf{f}_n$ is a generic expansion function (a tangential vector field), and $d_n$ is the corresponding expansion coefficient.

We remind the readers that in (2c) the test density $\mathbf{w}$ is an arbitrary tangential vector field. For simplicity, we admit that the test functions are equal to the expansion functions. Thus, we replace $\mathbf{w}$ in (2c) by the expansion function $\mathbf{f}_m$. We obtain

$$\begin{aligned}&-\left\langle\mathbf{f}_m\,|\,\hat{\mathbf{E}}\right\rangle_{\partial D} + \sum_n d_n\langle\mathbf{f}_m\,|\,\mathbf{f}_n\rangle_{\partial D,\Phi,G_1}\\ &\quad= \frac{1}{\beta^2}\sum_n d_n\langle\nabla_S\cdot\mathbf{f}_m\,|\,\nabla_S\cdot\mathbf{f}_n\rangle_{\partial D,\Phi}, \qquad m\text{ arbitrary}\end{aligned} \tag{18}$$

where $\langle\,|\,\rangle_{\partial D}$ is the scalar product over $\partial D$, and $\langle\,|\,\rangle_{\partial D,\Phi,G_1}$ and $\langle\,|\,\rangle_{\partial D,\Phi}$ are the following sesquilinear forms:

$$\begin{aligned}\langle\mathbf{h}_1\,|\,\mathbf{h}_2\rangle_{\partial D,\Phi,G_1} &= \int_{\partial D}\int_{\partial D}\mathbf{h}_1^*(\mathbf{r})\cdot\mathbf{h}_2(\mathbf{r}')\,\Phi_p(\mathbf{r}\,|\,\mathbf{r}')ds'ds\\ &\quad+\int_{\partial D}\int_{\partial D}\nabla_S\cdot\mathbf{h}_1^*\nabla_S'\cdot\mathbf{h}_2 G_1(\mathbf{r}\,|\,\mathbf{r}')ds'\end{aligned} \tag{19}$$

where $\mathbf{h}_1$ and $\mathbf{h}_2$ are generic vector fields and

$$\langle h_1\,|\,h_2\rangle_{\partial D,\Phi} = \int_{\partial D}\int_{\partial D}h_1^*(\mathbf{r})h_2(\mathbf{r}')\,\Phi_p(\mathbf{r}\,|\,\mathbf{r}')ds'ds \tag{20}$$

where $h_1$ and $h_2$ are generic scalar functions defined over $\partial D$. In Appendix C, we prove that the sesquilinear forms have hermitian symmetry and that $\langle\,|\,\rangle_{\partial D,\Phi}$ is a scalar product.

Substituting (7) and (17) into (16) and (18), we obtain the discretized form of the eigensystem (2) as follows:

$$\begin{aligned}&|\mathbf{k}_{\mathbf{I}}|^2 c_{\mathbf{I}}^r - \sum_n d_n\,\langle\mathbf{e}_{\mathbf{I}}^r|\,\mathbf{f}_n\rangle_{\partial D}\\ &\quad= \frac{|\mathbf{k}_{\mathbf{I}}|^4}{\beta^2}c_{\mathbf{I}}^r \qquad\qquad (21a)\\ &\qquad-\sum_{\mathbf{J}}\sum_{s=1,2}c_{\mathbf{J}}^s\,\langle\mathbf{f}_m\,|\mathbf{e}_{\mathbf{J}}^s\rangle_{\partial D} + \sum_n d_n\langle\mathbf{f}_m\,|\,\mathbf{f}_n\rangle_{\partial D,\Phi,G_1}\\ &\quad= \frac{1}{\beta^2}\sum_n d_n\langle\nabla_S\cdot\mathbf{f}_m\,|\,\nabla_S\cdot\mathbf{f}_n\rangle_{\partial D,\Phi} \qquad\qquad (21b)\end{aligned}$$

where $\mathbf{I}$ is an arbitrary multi-index, $r=1,2$, and $m$ is arbitrary.

The above equations form a generalized matrix eigensystem [20]. The eigenvalues are $1/\beta^2$, and the eigenvectors correspond to the coefficients $c_{\mathbf{J}}^1, c_{\mathbf{J}}^2$, and $d_n$ of the expansions (7) and (17). As discussed in Section III, the eigenvalues coincide with the resonant wavenumbers of (1).

Next we rewrite (21) in a matrix form. To this end, we define the matrices $\mathbf{\Lambda}=[\Lambda_{\mathbf{I},\mathbf{J}}]$, $\mathbf{T}^{(1)}=[T_{\mathbf{I},n}^{(1)}]$, $\mathbf{T}^{(2)}=[T_{\mathbf{I},n}^{(2)}]$, $\mathbf{P}=\lfloor P_{m,n}\rfloor$, and $\mathbf{Q}=\lfloor Q_{m,n}\rfloor$ as follows:

$$\Lambda_{\mathbf{I},\mathbf{J}} = |\mathbf{k}_{\mathbf{I}}|^2\delta_{\mathbf{I},\mathbf{J}} \tag{22}$$

$$P_{m,n} = \langle\nabla_S\cdot\mathbf{f}_m\,|\,\nabla_S\cdot\mathbf{f}_n\rangle_{\partial D,\Phi} \tag{23}$$

$$Q_{m,n} = \langle\mathbf{f}_m\,|\,\mathbf{f}_n\rangle_{\partial D,\Phi,G_1} \tag{24}$$

$$T_{\mathbf{I},n}^{(r)} = -\langle\mathbf{e}_{\mathbf{I}}^r\,|\,\mathbf{f}_n\rangle_{\partial D}, \qquad r=1,2. \tag{25}$$

We also define the following vectors: $\bar{\mathbf{c}}^{(1)}=[c_{\mathbf{J}}^1]$, $\bar{\mathbf{c}}^{(2)}=[c_{\mathbf{J}}^2]$, and $\bar{\mathbf{d}}=[d_n]$. It is clear that (21) is equivalent to the following generalized matrix eigensystem:

$$\begin{aligned}&\begin{pmatrix}\mathbf{\Lambda} & \mathbf{0} & \mathbf{T}^{(1)}\\ \mathbf{0} & \mathbf{\Lambda} & \mathbf{T}^{(2)}\\ \mathbf{T}^{(1)*} & \mathbf{T}^{(2)*} & \mathbf{Q}\end{pmatrix}\begin{pmatrix}\bar{\mathbf{c}}^{(1)}\\ \bar{\mathbf{c}}^{(2)}\\ \bar{\mathbf{d}}\end{pmatrix}\\ &\qquad= \frac{1}{\beta^2}\begin{pmatrix}\mathbf{\Lambda}^2 & \mathbf{0} & \mathbf{0}\\ \mathbf{0} & \mathbf{\Lambda}^2 & \mathbf{0}\\ \mathbf{0} & \mathbf{0} & \mathbf{P}\end{pmatrix}\begin{pmatrix}\bar{\mathbf{c}}^{(1)}\\ \bar{\mathbf{c}}^{(2)}\\ \bar{\mathbf{d}}\end{pmatrix}\end{aligned} \tag{26}$$

where $\mathbf{T}^{(r)*}$ stands for the Hermitian conjugate of $\mathbf{T}^{(r)}, r=1,2$.

The two matrices in (26) are self-adjoint. Indeed, $\mathbf{\Lambda}$ is real and diagonal, and, since the sesquilinear forms are Hermitian symmetric, the matrices $\mathbf{P}$ and $\mathbf{Q}$ are also self-adjoint, i.e., $\mathbf{P} = \mathbf{P}^*$ and $\mathbf{Q} = \mathbf{Q}^*$.

### *B. Solution of the Generalized Eigensystem*

In this section, we explain how the generalized eigensystem (26) is solved numerically. To begin with, we note that matrix $\mathbf{P}$ is nonnegative as follows:

$$\bar{\mathbf{d}}^* \cdot \mathbf{P} \cdot \bar{\mathbf{d}} \geq 0, \qquad \bar{\mathbf{d}} \text{ arbitrary.} \tag{27}$$

Indeed, from (23) we have

$$\begin{aligned} \bar{\mathbf{d}}^* \cdot \mathbf{P} \cdot \bar{\mathbf{d}} &= \sum_{n,m} d_m^* d_n P_{m,n} \\ &= \left\langle \nabla_S \cdot \sum_n d_n \mathbf{f}_n \,|\, \nabla_S \cdot \sum_n d_n \mathbf{f}_n \right\rangle_{\partial D, \Phi} \\ &\geq 0, \qquad \bar{\mathbf{d}} \text{ arbitrary.} \end{aligned} \tag{28}$$

The rightmost identity is a consequence of the sesquilinear form being a scalar product (see Appendix C). Thus, it is clear that $\bar{\mathbf{d}}^* \cdot \mathbf{P} \cdot \bar{\mathbf{d}} = 0$ if and only if $\sum d_n \nabla_S \cdot \mathbf{f}_n = 0$. This condition does not imply $\bar{\mathbf{d}} = 0$. In fact, the functions $\nabla_S \cdot \mathbf{f}_n$ are in general linearly dependent, in spite of the vector fields $\mathbf{f}_n$ being linearly independent. We conclude thus that in general $\mathbf{P}$ is degenerate, i.e., there is some vector $\bar{\mathbf{d}} \neq 0$ such that $\bar{\mathbf{d}}^* \cdot \mathbf{P} \cdot \bar{\mathbf{d}} = 0$.

A consequence of matrix $\mathbf{P}$ being degenerate is that it is not invertible. In particular, it follows that the matrix on the right-hand side of (26) is not invertible. This situation precludes the generalized eigensystem to be transformed into a standard eigenvalue problem.

To circumvent this drawback, we proceed as follows. So far, the expansion functions $\mathbf{f}_n$ were assumed to be arbitrary tangential fields. We admit hereafter that the expansion functions can be split into two sets. The functions in the first subset, $\mathbf{f}_n^{(1)} n = 1, 2, \ldots$, are such that $\nabla_S \cdot \mathbf{f}_n^{(1)}$ form a linearly independent set. The functions in the second subset, $\mathbf{f}_n^{(2)} n = 1, 2, \ldots$, are such that their surface divergence vanishes, i.e., $\nabla_S \cdot \mathbf{f}_n^{(2)} = 0$. Obviously, the set of all functions must be complete. An appropriate choice for the expansion functions is

$$\mathbf{f}_n^{(1)} = \nabla_S \varphi_n \quad \mathbf{f}_n^{(2)} = \hat{\boldsymbol{\nu}} \times \mathbf{f}_n^{(1)}, \qquad n = 1, 2, \ldots \tag{29}$$

where $\nabla_S$ is the surface gradient and $\varphi_0 = 1, \varphi_1, \ldots, \varphi_n, \ldots$, form a basis for the scalar functions over $\partial D$.

From the previous considerations, (17) becomes

$$\mathbf{f}(\mathbf{r}') = \sum_n d_n^{(1)} \mathbf{f}_n^{(1)}(\mathbf{r}') + d_n^{(2)} \mathbf{f}_n^{(2)}(\mathbf{r}'). \tag{30}$$

Vector $\bar{\mathbf{d}}$ is split into $\bar{\mathbf{d}} = [\bar{\mathbf{d}}^{(1)} \quad \bar{\mathbf{d}}^{(2)}]$. In the same way, the matrices $\mathbf{T}^{(1)}, \mathbf{T}^{(2)}, \mathbf{P}$, and $\mathbf{Q}$ are now written as

$$\begin{aligned} \mathbf{P} &= \begin{pmatrix} \mathbf{P}_{11} & \mathbf{P}_{12} \\ \mathbf{P}_{21} & \mathbf{P}_{22} \end{pmatrix} \\ \mathbf{Q} &= \begin{pmatrix} \mathbf{Q}_{11} & \mathbf{Q}_{12} \\ \mathbf{Q}_{21} & \mathbf{Q}_{22} \end{pmatrix} \\ \mathbf{T}^{(r)} &= \begin{bmatrix} \mathbf{T}_1^{(r)} & \mathbf{T}_2^{(r)} \end{bmatrix}, \qquad r = 1, 2. \end{aligned} \tag{31}$$

The submatrix $\mathbf{P}_{r,s} = \lfloor (\mathbf{P}_{r,s})_{m,n} \rfloor$, $r, s = 1, 2$, is defined as [compare with (23)]

$$(\mathbf{P}_{r,s})_{m,n} = \left\langle \nabla_S \cdot \mathbf{f}_m^{(r)} \,|\, \nabla_S \cdot \mathbf{f}_n^{(s)} \right\rangle_{\partial D, \Phi}. \tag{32}$$

The other submatrices are defined similarly. From the properties of the expansion functions, it is clear that $\mathbf{P}_{12} = \mathbf{P}_{21} = \mathbf{P}_{22} = \mathbf{0}$ and that $\mathbf{P}_{11}$ is positive definite. Moreover, $\mathbf{Q}_{11}$ and $\mathbf{Q}_{22}$ are self-adjoint, $\mathbf{Q}_{12} = \mathbf{Q}_{21}^*$, and $\mathbf{Q}_{22}$ is positive definite.

From the previous considerations, we conclude that (26) can be rewritten as

$$\begin{aligned} &\begin{pmatrix} \mathbf{\Lambda} & \mathbf{0} & \mathbf{T}_1^{(1)} & \mathbf{T}_2^{(1)} \\ \mathbf{0} & \mathbf{\Lambda} & \mathbf{T}_1^{(2)} & \mathbf{T}_2^{(2)} \\ \mathbf{T}_1^{(1)*} & \mathbf{T}_1^{(2)*} & \mathbf{Q}_{11} & \mathbf{Q}_{12} \\ \mathbf{T}_2^{(1)*} & \mathbf{T}_2^{(2)*} & \mathbf{Q}_{12}^* & \mathbf{Q}_{22} \end{pmatrix} \begin{pmatrix} \bar{\mathbf{c}}^{(1)} \\ \bar{\mathbf{c}}^{(2)} \\ \bar{\mathbf{d}}^{(1)} \\ \bar{\mathbf{d}}^{(2)} \end{pmatrix} \\ &\qquad = \frac{1}{\beta^2} \begin{pmatrix} \mathbf{\Lambda}^2 & \mathbf{0} & \mathbf{0} & \mathbf{0} \\ \mathbf{0} & \mathbf{\Lambda}^2 & \mathbf{0} & \mathbf{0} \\ \mathbf{0} & \mathbf{0} & \mathbf{P}_{11} & \mathbf{0} \\ \mathbf{0} & \mathbf{0} & \mathbf{0} & \mathbf{0} \end{pmatrix} \begin{pmatrix} \bar{\mathbf{c}}^{(1)} \\ \bar{\mathbf{c}}^{(2)} \\ \bar{\mathbf{d}}^{(1)} \\ \bar{\mathbf{d}}^{(2)} \end{pmatrix}. \end{aligned} \tag{33}$$

The last line of the matrix on the right-hand side of the above equation identically vanishes. As $\mathbf{Q}_{22}$ is invertible (because it is positive definite), the subvector $\bar{\mathbf{d}}^{(2)}$ can be written as a function of $\bar{\mathbf{c}}^{(1)}, \bar{\mathbf{c}}^{(2)}$, and $\bar{\mathbf{d}}^{(1)}$. Replacing $\bar{\mathbf{d}}^{(2)}$ in the remaining equations of the above system, we conclude that

$$\mathbf{A} \begin{pmatrix} \bar{\mathbf{c}}^{(1)} \\ \bar{\mathbf{c}}^{(2)} \\ \bar{\mathbf{d}}^{(1)} \end{pmatrix} = \frac{1}{\beta^2} \begin{pmatrix} \mathbf{\Lambda}^2 & \mathbf{0} & \mathbf{0} \\ \mathbf{0} & \mathbf{\Lambda}^2 & \mathbf{0} \\ \mathbf{0} & \mathbf{0} & \mathbf{P}_{11} \end{pmatrix} \begin{pmatrix} \bar{\mathbf{c}}^{(1)} \\ \bar{\mathbf{c}}^{(2)} \\ \bar{\mathbf{d}}^{(1)} \end{pmatrix} \tag{34}$$

where matrix $\mathbf{A}$ is given by

$$\begin{aligned} \mathbf{A} = &\begin{pmatrix} \mathbf{\Lambda} & \mathbf{0} & \mathbf{T}_1^{(1)} \\ \mathbf{0} & \mathbf{\Lambda} & \mathbf{T}_1^{(2)} \\ \mathbf{T}_1^{(1)*} & \mathbf{T}_1^{(2)*} & \mathbf{Q}_{11} \end{pmatrix} \\ &- \begin{bmatrix} \mathbf{T}_2^{(1)} \\ \mathbf{T}_2^{(2)} \\ \mathbf{Q}_{12} \end{bmatrix} \mathbf{Q}_{22}^{-1} \begin{bmatrix} \mathbf{T}_2^{(1)*} & \mathbf{T}_2^{(2)*} & \mathbf{Q}_{12}^* \end{bmatrix}. \end{aligned} \tag{35}$$

The matrices in (34) are self-adjoint. Moreover, the matrix on the right-hand side is positive definite and thus invertible. Hence, the eigensystem (34) can be transformed into a standard eigenvalue problem. The eigenvalues are $1/\beta^2$ and correspond to the resonant wavenumbers of (1).

The inversion of the positive definite matrix in (34) breaks the Hermitian symmetry of the system. This is undesirable because the numerical computation of the spectrum of a self-adjoint matrix is much more efficient than the computation of the spectrum of a generic matrix. To avoid losing the Hermitian symmetry of the system, we can alternatively factorize the right-hand-side matrix using the Cholesky algorithm and then proceed as explained in [20].

We have thus proven that the calculation of the band structure of a metallic crystal can be reduced into a standard matrix eigenvalue problem. Due to the smoothness of the vector field $\tilde{\mathbf{E}}$, the plane-wave expansion (7) converges fast, and only a few terms are needed to obtain very accurate results for the first few bands. Under these circumstances, most of the computational effort is related to the calculation of the matrix entries

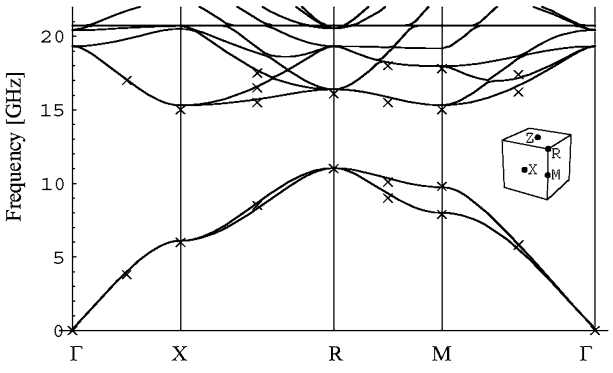


Fig. 2. Band structure of a simple cubic lattice of nearly touching metallic spheres embedded in air. The $\times$-points correspond to data extracted from [21]. The points $\Gamma, X, M$, and $R$ are defined as usual [21].

in (34). This computational effort is comparable to that required for characterizing a single metallic inclusion using the MoM.

## V. Numerical Examples

The objective of this section is to validate the proposed method and discuss its efficiency and computation time. We investigate propagation in media with sphere- and disk-type inclusions, media with wire inclusions (long thin dipoles and the 3-D wire medium), and left-handed media (two different structures similar to Smith's original configuration [4]).

### A. Media With Spherical Inclusions

In order to validate the method, we study the propagation of electromagnetic waves in a structure that consists of an array of metallic spheres arranged into a simple cubic lattice. The lattice constant is $a = 13.4$ mm and the diameter of the spheres is $2R = 12.7$ mm. In [21], the band structure of this metallic crystal was computed numerically using a multiple scattering technique (which involves the computation of the zeros of a nonlinear equation). The comparison of numerical data and experimental results is also presented in [21].

We computed the band structure of the same artificial material using the hybrid method proposed in this paper. We expanded the unknown surface current in vector spherical harmonics [19, p. 170] (the scalar functions $\varphi_n$ in (29) are taken to be equal to spherical harmonics $Y_l^m$; we considered that $l \leq 5$ in the simulations, i.e., 70 vector functions). The auxiliary field is expanded into 686 plane waves. The computation time is about 5 min for each wave vector on a standard personal computer (Pentium III 800 MHz). Most of the computation time is spent assembling the $\mathbf{P}$ and $\mathbf{Q}$ matrices; in [21], the computation time is not given.

In Fig. 2, we show our results superimposed on data extracted from ([21, Fig. 1]) (the $\times$-points; the frequency range of the results of [21] is limited to $0 < f < 18$ GHz). The agreement is very good. Note that the considered test example is extremely demanding because the metallic spheres nearly touch and so the induced current has strong variations over the inclusion's surface (this is why we had to consider so many expansion functions). There is a complete bandgap between the second and third bands [21].

As depicted in Fig. 2, there is a flat band around $f = 20.73$ GHz (indeed it is a triply degenerate flat band). This flat band corresponds to the lowest frequency of resonance of the spherical cavity. It occurs at the free-space wavenumber $\beta = 2.7437/R$, where $R$ is the radius of the spheres [22, p. 385] (this frequency is the zero of an equation involving spherical Bessel functions). Thus, theoretically, the lowest (internal) frequency of resonance for the considered spherical inclusions is $f = 20.63$ GHz. This value agrees very well with the one obtained from our numerical computations (the error is 0.05%). This further validates the proposed method. As discussed in Section II, the internal resonant frequencies do not belong to the band structure of the periodic medium and thus must be removed. We did not remove these bands merely to illustrate that they can be easily detected in the computed results by direct inspection. Alternatively, a scheme analogous to that described in our previous paper [9] can be implemented. We stress that, if the volume fraction of the inclusions $f_V$ is not too high, the internal resonant frequencies of the associated cavity do not interfere with the first few modes of the periodic material.

We also obtained an excellent agreement in the long-wavelength limit with the model described in [22, p. 763] for dilute mixtures (the effective index of refraction of the material is written in terms of the electric and magnetic polarizabilities of a sphere and using an interaction constant; the exact value for the interaction constant is $1/3a^3$ [18]). Indeed, for the volume fraction $f_V = 1\%$, we obtained from the slope of the dispersion characteristic at the $\Gamma$-point that $\varepsilon_{\text{eff}}\mu_{\text{eff}} = 1.014926$ (using 250 plane waves and 6 expansion functions for the surface current), whereas the result predicted by the formulation of [22] is $\varepsilon_{\text{eff}}\mu_{\text{eff}} = 1.014925$.

### B. Media With Finite-Length Wire Inclusions

In this section, we characterize the propagation of electromagnetic waves in the so-called wire medium. The inclusions are long, thin, straight metallic wires. The wire medium was initially proposed in the artificial dielectric context [23], but recently it was pointed out that its frequency-polarization-angle selective properties might find other interesting applications [24].

In [23], the periodic MoM is utilized to determine the effective permittivity of the wire medium. The dispersion characteristic of the artificial medium is determined by setting the determinant of an impedance matrix to zero (i.e., the problem is reduced to finding the zeros of a nonlinear equation). In [24], an approximate periodically loaded transmission-line model is used to characterize the wire medium.

The numerical results presented here were obtained by solving (34) using the thin-wire approximation. In this way, we admit that electric current (which as referred before is proportional to the vector density $\mathbf{f}$) flows along the wires and is constant in the cross section. We expand $\mathbf{f}$ in triangular subdomain functions $\mathbf{f}_n = \Delta_n \hat{\mathbf{u}}_3$ ($\Delta_n$ is a triangular subdomain function; it vanishes at the ends of the wire). Within the thin-wire approximation, the splitting of the expansion functions described in Section IV-B is not necessary because the set $\nabla_S.\mathbf{f}_n$ is linearly independent. This situation does not occur in the general case in which the variation of the current in the cross section is not neglected.

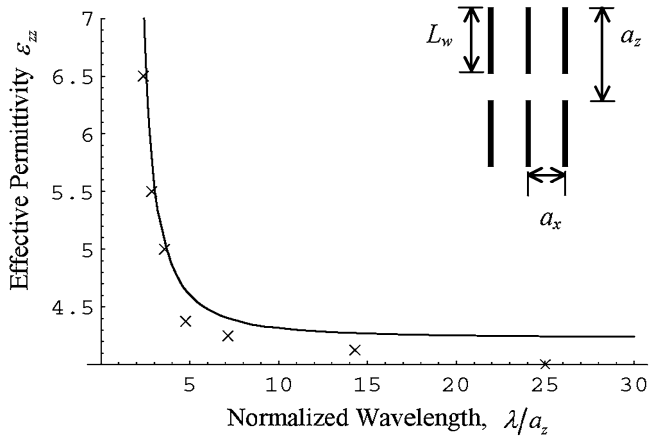


Fig. 3. Effective permittivity of the wire medium as a function of the normalized wavelength, superimposed on results (×-points) extracted from [23]. The geometry is described in the text.

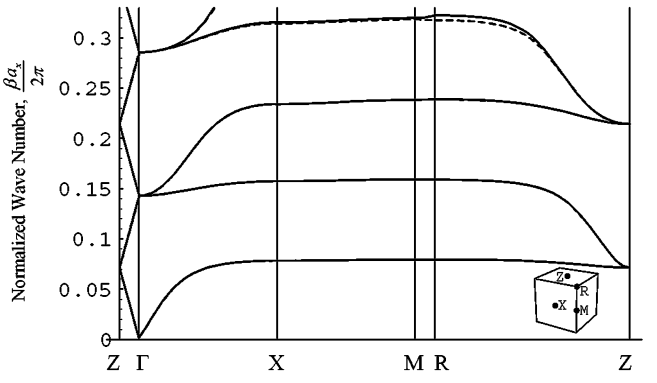


Fig. 4. Band structure for the $E$-polarized waves (125 plane waves: solid line; 729 plane waves: dashed line). The geometry is described in the text.

We admit that the wires are arranged into an orthogonal lattice and stand in air. The primitive vectors are $\mathbf{a}_1 = (a_x, 0, 0), \mathbf{a}_2 = (0, a_x, 0)$, and $\mathbf{a}_3 = (0, 0, a_z)$. A generic wire has length $L_w$ and radius $a_w$. The geometry of the unit cell is analogous to that depicted in Fig. 1, with the wire axis oriented along the $x_3$ direction.

We discretized the current density with 16 basis functions and the auxiliary field $\tilde{\mathbf{E}}$ with 125 plane waves. The typical computation time for each wave vector is about 1 min.

In order to validate the numerical implementation of the method, we compute the effective permittivity of the wire medium. We admit that the wire length is $L_w = 0.86a_z$, the wire radius is $a_w = 0.1a_x$, and $a_z = 7a_x$. The relative permittivity in the $x_3$ direction, $\varepsilon_{zz}$, is computed from the slope of the dispersion characteristic in the $\Gamma X$ segment of the Brillouin zone [1], where $\Gamma$ is the origin and $X = (\pi/a_x, 0, 0)$. The calculated results are depicted in Fig. 3. We superimposed on our results data extracted from [23, Fig. 3]. The agreement is satisfactory. The small discrepancy for long wavelengths is probably due to the results of [23] having not reached convergence. This is suggested by the variation of the permittivity curves with the number of expansion functions in [23].

The calculated permittivity is almost insensitive to the number of terms in the plane-wave expansion as we increase the number of plane waves from 1 (with wave vector $\mathbf{k}$ and polarization parallel to the wires) up to 729. At least the first digit after the decimal point in $\varepsilon_{zz}$ remains unchanged in such a situation. This is due to the smoothness of the auxiliary field, which ensures that the Fourier series converges quickly. The error is larger for high frequencies. The described situation clearly proves the efficiency of the proposed method. We note that the standard plane-wave method (which only applies to the dielectric case) does not have this property by any means. The convergence of the plane-wave method may be very poor, even in the static limit [25].

For long wavelengths, we obtained $\varepsilon_{zz} = 4.23$ in excellent agreement with the static homogenization method proposed by the authors in [26]. For $\lambda/a_z > 10$, the permittivity is practically independent of frequency. For $\lambda/a_z = 1.82$, a bandgap emerges, and the permittivity becomes complex. A good estimate for the frequency range where the homogenization results apply is $\lambda > 2\sqrt{\varepsilon_{zz}}a_z$ [26].

It can be easily verified that within the thin-wire approximation the plane waves with polarization normal to the wires ($H$-polarized waves) propagate undisturbed in the wire medium. The $H$-polarized plane waves are thus Floquet modes in the wire medium. We name the remaining Floquet modes as "$E$-polarized modes." The results presented in this section refer exclusively to the $E$-polarized modes. Based on the free-space case, we expect that the minimum number of plane waves required for computing the first $2N + 1$ bands of the $E$-polarized modes is approximately $(2N + 1)^3$ (we remove the $H$-polarized waves from the plane-wave expansion, and for simplicity we consider that the sum range in (7) is the same in the indexes $j_1, j_2$, and $j_3$). Thus, to calculate the first five bands, we need at least 125 plane waves.

In Fig. 4, we depict the band structure calculated with 125 plane waves (solid line) superimposed on the band structure calculated with 729 plane waves (dashed line). The inset of the figure represents the Brillouin zone, and $Z = (0, 0, \pi/a_z), M = (\pi/a_x, \pi/a_x, 0)$, and $R = (\pi/a_x, \pi/a_x, \pi/a_z)$.

As seen in Fig. 4, there is practically no difference between the solid line and dashed line results. Only in the fourth band is some discrepancy perceptible. The results illustrate that the proposed method allows calculating the dispersion characteristic of artificial materials accurately, with a number of plane waves very close to the minimum.

The dispersion characteristic along the segments $\Gamma X$ and $XM$ shows that the wire medium has large bandgaps for the considered polarization, and propagation in the $\Gamma XM$ plane (normal to the wires). The first bandgap is defined by $0.078 < \beta a_x/2\pi < 0.143$. Along the $\Gamma Z$ direction (i.e., along the wires), there is no bandgap since the free-space plane waves propagate undisturbed.

### C. 3-D Wire Medium

In this section, we investigate the propagation characteristics in the 3-D wire structure depicted in Fig. 5. This structure consists of an array of metallic wires with infinite length. The wires are oriented along the coordinates axes and form a simple cubic lattice with lattice constant $a$ (the lattice constant is the smallest

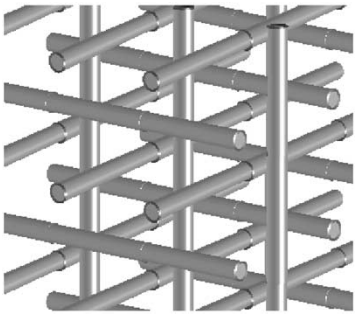

Fig. 5. Geometry of the 3-D wire medium.

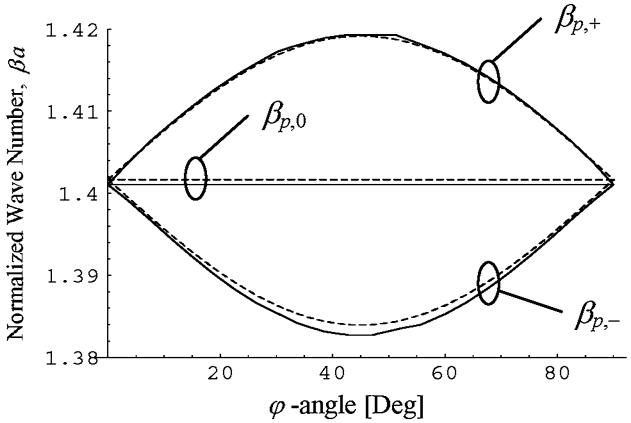


Fig. 6. Normalized wavenumber for the plasma bands as a function of the $\varphi$ angle. The solid lines correspond to numerical results and the dashed lines correspond to the theoretical model discussed in the text.

distance between parallel wires; we consider that the distance between adjacent perpendicular wires is half-lattice constant).

The characterization of the 3-D wire medium is important because apparently it behaves as an ideal isotropic material with negative permittivity in the long-wavelength limit [27]. This has important applications in the left-handed media context [4], [29] (see Section V-D).

It is commonly accepted [4] that for long wavelengths the wire medium can be described by the (relative) effective permittivity $\varepsilon_{\text{eff}} = 1 - \beta_0^2/\beta^2$, where $\beta_0 = \omega_0/c$ and $\omega_0$ is the plasma frequency. However, recent results [28] suggest that this model may insufficient to describe the electrodynamics of the 3-D wire medium. Indeed, in [28] it was proven that the one-dimensional (1-D) wire medium is characterized by strong spatial dispersion in the long-wavelength limit (i.e., the permittivity depends explicitly on the wave vector). The 1-D wire medium is a metamaterial in which the wires are all oriented in the same direction. In [28], it was proven that $\varepsilon_{zz} = 1 - \beta_0^2/(\beta^2 - k_z^2)$, where $\varepsilon_{zz}$ is the component of the permittivity dyadic along the direction of the wires (the permittivity dyadic evaluates to unity in the transverse directions).

The objective of this section is to assess numerically if the classic plasma model describes accurately the wave propagation in the 3-D wire medium. To our best knowledge, the unique band structure analysis of the 3-D wire medium published in the literature is based on experimental data [27] (the topology of the structure described in [27] is slightly different from the one considered here).

We applied the method proposed in this paper to compute the dispersion characteristic of the 3-D wire medium. We used the thin-wire approximation described in the previous section. The surface current over the three wire sections in the unit cell was expanded into 15 expansion functions (the current over each wire is now a Floquet wave). The wire radius is $a_w = 0.01a$. We restrict our attention to wave propagation in the $x_3 = 0$ plane. In the simulations, we assume that the wave vector is of the form $\mathbf{k} = |\mathbf{k}|(\cos\varphi, \sin\varphi, 0)$ with $|\mathbf{k}| = 0.1\pi/a$. We computed the resonant frequencies of the 3-D wire medium as a function of the $\varphi$ angle (which defines the direction of the wave vector). We are interested uniquely in the long-wavelength limit. The simulation results show that in the long-wavelength limit there are five relevant electromagnetic modes. Two electromagnetic modes propagate only at frequencies much smaller than the plasma frequency of the metamaterial. The study of these two modes is beyond the scope of the present paper and will be discussed elsewhere. Near the plasma frequency, the simulation results show that three distinct electromagnetic modes propagate. The dispersion characteristic of these three modes is depicted in Fig. 6 as a function of the $\varphi$ angle (solid line curves).

It is now appropriate to compare the numerical results with the standard plasma model. As is well known [1, p. 162], the plasma model predicts that the electromagnetic modes are transverse electromagnetic with the dispersion characteristic $\beta_{p,0}^2 = \beta_0^2 + |\mathbf{k}|^2$. There is also a dispersionless band $\beta = \beta_0$ associated with longitudinal modes [1]. Thus, since we considered that $|\mathbf{k}|$ was constant, the computed dispersion characteristic *should* be flat. As seen in Fig. 6, only the second band is flat, and it actually compares very well with $\beta_{p,0}$, which is shown as a dashed line in Fig. 6 (the plasma frequency was computed, as explained in [28] and is approximately $\beta_0 a \approx 1.37$). Why is there a discrepancy in the other bands?

Based on the results of [28], it seems reasonable to assume (provided the orthogonal wires do not interact significantly) that the permittivity dyadic in the 3-D wire medium is diagonal and evaluates to $\varepsilon_{i,i} = 1 - \beta_0^2/(\beta^2 - k_i^2)$ in the $x_i$ direction. We investigated if this theoretical model does describe the electrodynamics of the 3-D wire medium. To this end, we inserted the permittivity dyadic in the well-known dispersion model for electromagnetic waves in anisotropic media [22, p. 202], and then we solved the equation in the vicinity of $\beta = \beta_0$ (we calculated the first term of the Taylor series of the solutions in powers of $|\mathbf{k}|$). Assuming that $k_z = 0$, we found that the theoretical model predicts the existence of three electromagnetic modes near the plasma frequency. The theoretical dispersion characteristic of the modes is $\beta_{p,0}^2 = \beta_0^2 + |\mathbf{k}|^2$, $\beta_{p,+}^2 = \beta_0^2 + |\mathbf{k}|^2 + k_x k_y$, and $\beta_{p,-}^2 = \beta_0^2 + |\mathbf{k}|^2 - k_x k_y$. In Fig. 6 we depict the results predicted by the theoretical model (dashed lines) superimposed on the numerical data. The agreement is excellent, and thus it seems that the proposed model accurately describes the 3-D wire medium.

We have also computed the polarization of the average fields numerically (we calculated the eigenfunctions of the eigensystem (1); the eigenfunctions were averaged over the unit cell). The polarization of the mode with dispersion $\beta_{p,0}$ is along the $z$ axis (the wave is transverse electromagnetic). On the other hand, the polarization of the mode with dispersion

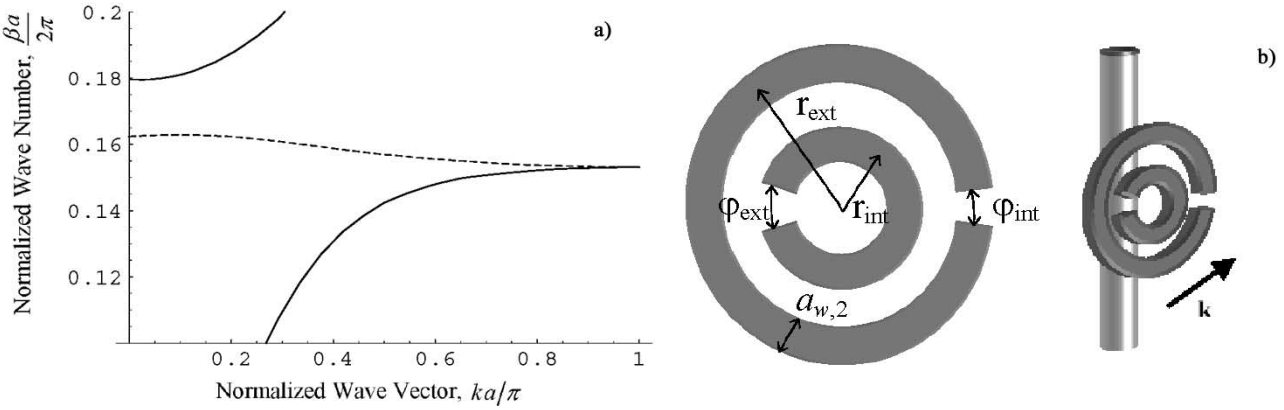


Fig. 7. (a) Dispersion characteristic of the SRRs (solid line) and SRRs + wires (dashed line). (b) Geometry of the crystal and of the SRR particle.

$\beta_{p,\pm}$ is roughly independent of the wave vector direction: $\mathbf{E}_{\text{av},\pm} \propto (1, -(\pm 1), 0)$. Note that the described results assume always that $k_z = 0$. It can be proven that the results are consistent with proposed permittivity model. In the particular case in which the wave vector is along a coordinate axis, the three electromagnetic modes are degenerate. Two modes can be taken as transverse, and a third mode can be taken as longitudinal (the existence of a longitudinal mode was also suggested in [27] based on experimental data). From the results described here, it is apparent that the propagation in the wire medium is much more intricate than it was thought and that there is no isotropy near the plasma frequency. This new result may have important consequences in the left-handed media context. A detailed study of the wave propagation in the 3-D wire medium, together with an analytical proof that further justifies the proposed permittivity model, will be presented elsewhere.

### *D. Left-Handed Media*

In recent years, the study of periodic structures in the long-wavelength limit regained interest after the extraordinary breakthrough that it is possible to synthesize a material having simultaneously negative permittivity and permeability over a certain frequency band [4]. These materials are known as left-handed or double negative materials, and their unconventional electrodynamics were investigated a long time before they were actually discovered [29]. In this section, we characterize artificial materials with a topology equivalent to that described in [4] and [30] and briefly discuss bianisotropic effects.

In the first example, the unit cell contains a wire section and a split-ring resonator (SRR), as illustrated in Fig. 7(b). The radius of the wire is $a_{w,1} = 0.1a$, which corresponds to the plasma normalized frequency $\beta_0 a/2\pi \approx 0.38$. The periodic structure resembles that of Smith *et al.*'s [4]. The main difference is that to ease the numerical implementation we considered that the SRR consists of two concentric tori instead of planar rings. The tori geometry is shown in Fig. 7(b). The radii of the inner and exterior tori are consistent with the (half-width) radii of the rings in [4] ($r_{\text{int}} = 0.2375a$ and $r_{\text{ext}} = 0.3625a$). The gapwidths $\varphi_{\text{int}} = 15.28°$ and $\varphi_{\text{ext}} = 9.17°$ are not specified in [4] and so may not agree with our choices. The tori cross section is characterized by the radius $a_{w,2} = 0.05a$ (the diameter of the cross section is the same as the width of the rings in [4]).

We assume propagation in the direction indicated in Fig. 7(b). We computed the dispersion characteristic of the metamaterial first without the wires (solid line) and then with the wires and the SRR particles (dashed line). The result for the relevant electromagnetic mode is depicted in Fig. 7(a).

Our results are qualitatively equivalent to those described in [4]. When the wires are added to the crystal, a new band emerges in a frequency region previously forbidden (where the SRR particles see a negative permeability). The slope of the dispersion characteristic shows that the composite medium is characterized by left-handed behavior. The lower edge of the new band corresponds to the free-space wavelength $\lambda = 6.5a$. The corresponding value for the SRR particle considered in [4] is $\lambda = 8.9a$.

As seen in Fig. 7, the new band does not completely occupy the bandgap of the SRR crystal. In [30], it was shown that this effect can be explained in terms of the bianisotropy of the SRR particle. To avoid bianisotropy, a modification of the standard SRR was proposed in [30] (the modified split-ring resonator (MSRR) particle). This particle consists of two parallel rings with the same radius (as before, each ring has a gap and the gaps are rotated by 180°). Based on analytical results, it was predicted that a crystal with wires and MSRR particles has left-handed behavior and no bianisotropy. Thus, within this model, the dispersion characteristic of a medium with wires and MSRR particles occupies completely the bandgap of the crystal without wires.

We tried to assess numerically the validity of the theory described above. As before, we modeled each ring with a torus section. The dimensions of the two rings are same as the dimension of the exterior ring in the previous example. The distance between the tori is $d = 0.025a$. The computed dispersion characteristic is depicted in Fig. 8. As predicted by Marqués *et al.* [30], the gap is now completely occupied by the dispersion characteristic of the composite structure. The lower edge of the new band occurs now at $\lambda = 7.7a$. We have also computed the average electromagnetic fields, and using that information we were able to further verify that the first structure discussed in this section suffers from bianisotropic effects, whereas the second does not. The results and a more detailed discussion will be presented elsewhere.

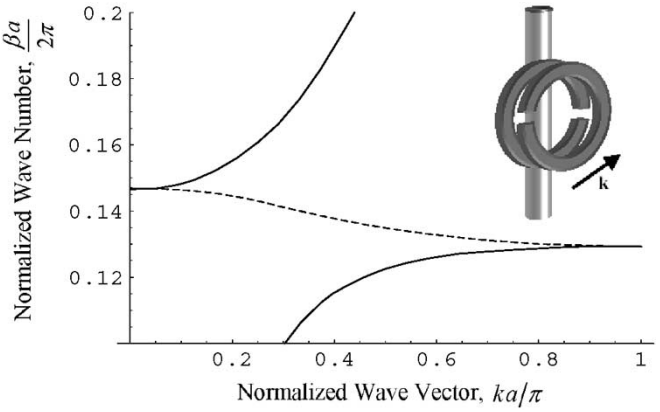


Fig. 8. Dispersion characteristic of the MSRR (solid line) and MSRR + wires (dashed line). The inset of the figure illustrates the geometry of the crystal.

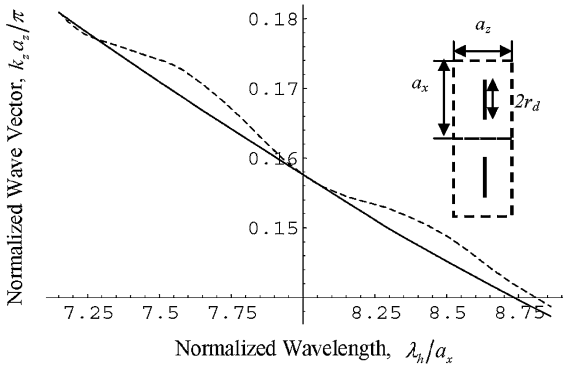


Fig. 9. Normalized longitudinal wave vector as a function of the normalized host material wavelength (solid line: calculated results; dashed line: experimental data).

### *E. Media With Disk-Type Inclusions*

The disk-type medium consists of a 3-D array of metallic disks with radius $r_d$. The thickness of the disks is assumed to be negligible. The filtering properties of the disk-type material were used in [6] to design monolithic waveguide filters. In this paper, we study the bandgap width as a function of the lattice parameters for normal incidence.

Before that, we present experimental data that further validates the hybrid method presented in this work. We fabricated a sample of the disk-type material with cross section $A_x \times A_y = 22.8\,\text{mm} \times 10\,\text{mm}$ and length $l = 16.05$ mm. The sample consists of 10 layers of disks. Each layer consists of an $8 \times 4$ rectangular array of metallic disks imprinted on a dielectric slab with relative permittivity $\varepsilon_h/\varepsilon_0 = 2.2$ (RT/Duroid). The area fraction of the disks (relative to the cross section of the sample) is 44.1%. The sample is inserted into an $X$-band rectangular waveguide terminated in a short circuit (the sample completely fills the waveguide cross section). The geometry is similar to the one considered in [6].

From frequency swept waveguide measurements, we obtained the reflection coefficient at the air-sample plane (the sample is illuminated with the $\text{TE}_{10}$ fundamental mode). The frequency span was 8–10 GHz. This frequency band corresponds to $7.10 < \lambda_h/a_1 < 8.87$, where $\lambda_h$ is the radiation wavelength in the host dielectric material (the experimental procedure described here is only appropriate to characterize the long-wavelength regime). The measured reflection coefficient data can be used to obtain the dispersion characteristic of the artificial material. Indeed, we can assume to a first approximation that the propagation in the sample is described by an unknown propagation constant $k_z$ and by the transverse wave impedance $Z_{\text{TE}} = \omega\mu_0/k_z$ (the formula is obvious from the theory of metallic waveguides [22]). The reflection coefficient at the air-sample plane can be easily written in terms of the unknown $k_z$. Thus, from the experimental data, we can compute $k_z$ as a function of the frequency. We compared the measured $k_z$, with the one calculated using the hybrid method (in the simulations the medium is modeled as a crystal with primitive vectors such that $a_x = A_1/8, a_y = A_2/4$, and $a_z = l/10$; the wave vector is of the form $\mathbf{k} = (\pi/A_1, 0, k_z)$, the notation being evident). The results are depicted in Fig. 9. The agreement is good, except for some irregular behavior in the measured data mainly related to imperfections in the experimental setup.

We have also compared our simulation results with those obtained using the transmission-line model described in [6] and [22]. The transmission-line model allows characterizing the bandgap properties of the structure, provided that the disk area fraction is moderate and the disk planes are sufficiently distant so that single-mode propagation can be assumed. We found good agreement for the first few bands. The comparison is not presented here for conciseness.

Unlike the transmission-line models presented in [6] and [22], our full wave results allow characterizing the dispersion characteristic of the artificial material for closely packed disks and large radii. As discussed in [6], these configurations have very good filtering properties. In the rest of this section, we investigate numerically how the bandgap is affected by the distance between the disk planes.

We consider that the disk area fraction is 50%. In each layer, the disks are arranged into a square lattice with lattice constant $a_x$. The distance between adjacent disk planes is $a_z$. We study two distinct configurations: either the disk planes are aligned or alternatively the disks are shifted by a half lattice constant (in this case, $\mathbf{a}_3 = (0.5a_x, 0.5a_x, a_z)$).

The electric current over the disk surface is expanded using Chebyshev polynomials (radial coordinate) and complex exponentials (angular coordinate). The boundary edge singularity of the current is taken explicitly into account to improve the convergence rate of the method. The details of the implementation and an appropriate splitting basis are described in [18]. The results presented here were obtained with 250 plane waves and 42 expansion functions. The computation time for each wave vector is approximately 2 min. Since the inclusions are planar, the structure has no internal resonant frequencies (thus, no flat bands occur in the calculated band structure).

We computed the bandgap between the second and third bands for normal incidence (i.e., propagation is along the direction normal to the disks or, equivalently, the wave vector is restricted to the $\Gamma Z$ segment of the Brillouin zone). The corresponding gap–midgap ratio, defined as the quotient between the bandgap width and the center frequency, is depicted in Fig. 10 as a function of the normalized distance $a_z/a_x$. The gap–midgap ratio increases as the disk planes are brought

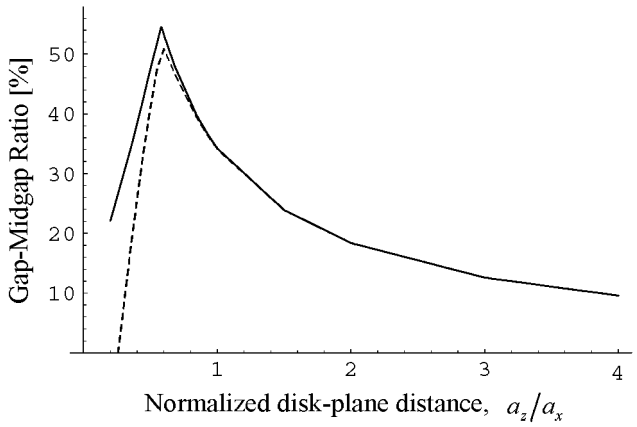


Fig. 10. Gap–midgap ratio as a function of the normalized disk-plane distance for normal incidence (solid line: aligned planes; dashed line: shifted planes). The disk-area fraction is 50%.

together, provided that $a_z > 0.6a_x$. For smaller distances, the gap–midgap ratio decreases quickly down to zero.

For $a_z > 0.9a_x$, the gap–midgap ratio is practically independent of the relative position of the disk planes. For smaller distances, the gap–midgap ratio for aligned disk planes is larger than that for shifted disk planes. Thus, the aligned disk-plane configuration favors the band-gap opening in the normal direction. The results predict that the optimal distance for a large bandgap is $a_z \approx 0.6a_x$. In general, both the low– and high-frequency limits of the bandgap increase as the disk planes are brought together. The upper edge of the bandgap can be estimated using the formula $\beta = \pi/a_z$ (the formula is very accurate for $a_z > 0.6a_x$). The optimal distance decreases slowly with the disk area.

## VI. Conclusion

In this paper, we extended the hybrid method proposed in [9] to the 3-D metallic case. The 3-D case is much more elaborate because the vector nature of radiation complicates considerably the smoothing of the electromagnetic fields with layer potentials. We have proven that the band structure problem is equivalent to an auxiliary integral-differential eigensystem that can be conveniently solved using the plane-wave method and the MoM. Unlike other root-searching-based methods proposed in the literature [21], [23], our formalism reduces the problem to a standard matrix eigensystem. This approach is much more effective, since for one side all of the eigenvalues are obtained at once, and on the other side there is no possibility of missing solutions. Numerical results and computation time show that the method is very efficient and thus may contribute to the characterization of emerging artificial materials. Most of the numerical effort is related to the assembly of the MoM matrix. We stress that the standard plane-wave method cannot, to the best of our knowledge, be directly applied to dispersionless metallic structures, and so we believe that our method is an important contribution to redeem that shortcoming. To illustrate the application of the developed formalism, we investigated wave propagation in several relevant periodic structures, which include disk-, wire-, and sphere-type media and metamaterials that exhibit left-handed behavior. The validity of the plasma model in the 3-D wire medium and the role of bianisotropy in left-handed materials were discussed. We also studied the variation of the bandgap width with lattice parameters in the disk-type medium. The method was extensively validated against the open literature and with experimental data.

## Appendix A

Here, we explain how the Green's functions introduced in Section III can be efficiently calculated. The solution of (3) (the lattice Green's function) has the following spectral representation [18]:

$$\Phi_p(\mathbf{u}) = \frac{1}{V_{\text{cell}}} \sum_{\mathbf{J}} \frac{e^{-j\mathbf{k_J}.\mathbf{u}}}{|\mathbf{k_J}|^2}$$
$$\mathbf{k_J} = \mathbf{k} + j_1\mathbf{b}_1 + j_2\mathbf{b}_2 + j_3\mathbf{b}_3 \tag{A1}$$

where $\mathbf{u} = \mathbf{r} - \mathbf{r}'$, $V_{\text{cell}} = |\mathbf{a}_1.\mathbf{a}_2 \times \mathbf{a}_3|$ is the volume of the unit cell, $\mathbf{J} = (j_1, j_2, j_3)$ is a multi-index of integers, and $\mathbf{b}_1, \mathbf{b}_2$, and $\mathbf{b}_3$ are the reciprocal lattice primitive vectors. The above representation converges slowly and is of very limited interest in the numerical evaluation of the Green's function. A more preferable representation for the Green's function is the mixed-domain representation proposed by the authors in [16] (which is coincident with that of [17] for the case considered here). The result is

$$\Phi_p = \frac{1}{V_{\text{cell}}} \sum_{\mathbf{J}} \left( \frac{e^{-|\mathbf{k_J}|^2/4E^2}}{|\mathbf{k_J}|^2} e^{-j\,\mathbf{u}.\mathbf{k_J}} \right) + \sum_{\mathbf{I}} \frac{1}{4\pi\rho_{\mathbf{I}}} \big(1 - \text{erf}(E\rho_{\mathbf{I}})\big) e^{-j\,\mathbf{k}.\mathbf{r_I}} \tag{A2}$$

where erf is the error function, $\mathbf{u} = \mathbf{r} - \mathbf{r}', \rho_{\mathbf{I}} = |\mathbf{u} - \mathbf{r_I}|$, and $\mathbf{r_I} = i_1\mathbf{a}_1 + i_2\mathbf{a}_2 + i_3\mathbf{a}_3$. The symbols $\mathbf{I}$ and $\mathbf{J}$ stand for a generic triple-index. The $E$ parameter is an arbitrary positive constant that defines the relative convergence rate of the spatial-like parcel (the sum with index $\mathbf{I}$) and the spectral-like parcel (the sum with index $\mathbf{J}$). A good choice for the $E$ parameter, which ensures a similar convergence rate for the spatial-like and spectral-like sums, is $E = \sqrt{\pi}/V_{\text{cell}}^{1/3}$. The mixed-domain representation has, irrespective of the observation point, Gaussian convergence. Therefore, it has an excellent convergence rate. Alternative representations for the Green's function and a more complete discussion on this topic can be found in [16] and [18].

The spectral representation of the Green's function $G_1$, the solution of (4), is given by

$$G_1(\mathbf{u}) = -\frac{1}{V_{\text{cell}}} \sum_{\mathbf{J}} \frac{e^{-j\mathbf{k_J}\cdot\mathbf{u}}}{|\mathbf{k_J}|^4}. \tag{A3}$$

This result can be verified by direct substitution in (4) using (A1). Again the spectral representation converges slowly and is not appropriate for the numerical evaluation of $G_1$. Next we obtain an alternative mixed-domain representation for the Green's function with Gaussian convergence rate. More specifically, we propose a solution of the form

$$G_1 = -\frac{1}{V_{\text{cell}}} \sum_{\mathbf{J}} \left( \frac{e^{-|\mathbf{k_J}|^2/4E^2}}{|\mathbf{k_J}|^4} e^{-j\mathbf{u}\cdot\mathbf{k_J}} \right) + \sum_{\mathbf{I}} G_0(\rho_{\mathbf{I}}) e_{\mathbf{I}}^{-j\,\mathbf{k}\cdot\mathbf{r}} \tag{A4}$$

where $G_0 = G_0(r)$ is some function to be determined and $r = |\mathbf{r}|$. Inserting the above formula into (4) and comparing with (A2), it is clear that $G_0$ must satisfy

$$\nabla^2 G_0 = \frac{1}{4\pi r}\big(1 - \operatorname{erf}(Er)\big). \tag{A5}$$

The solution of (A5) is given by

$$G_0(r) = \frac{1}{4\pi}\left(-\frac{e^{-(Er)^2}}{2E\sqrt{\pi}} + \frac{1}{2}r\big(1 - \operatorname{erf}(Er)\big) - \frac{1}{4E^2}\frac{\operatorname{erf}(Er)}{r}\right). \tag{A6}$$

If we insert the above formula into (A4), the series with index $\mathbf{I}$ converges quickly, except for the term associated with the third parcel in (A6). However from (A2), it is easy to verify that (see also [16]–[18])

$$\sum_{\mathbf{I}} \frac{1}{4\pi\rho_{\mathbf{I}}}\operatorname{erf}(E\rho_{\mathbf{I}})e^{-j\mathbf{k}\cdot\mathbf{r}_{\mathbf{I}}} = \frac{1}{V_{\text{cell}}}\sum_{\mathbf{J}}\left(\frac{e^{-|\mathbf{k}_{\mathbf{J}}|^2/4E^2}}{|\mathbf{k}_{\mathbf{J}}|^2}e^{-j\,\mathbf{u}\cdot\mathbf{k}_{\mathbf{J}}}\right). \tag{A7}$$

Therefore, we conclude that $G_1$ can be calculated using the following mixed representation:

$$G_1 = -\frac{1}{V_{\text{cell}}}\sum_{\mathbf{J}}\left(\frac{1}{|\mathbf{k}_{\mathbf{J}}|^4} + \frac{1}{4E^2|\mathbf{k}_{\mathbf{J}}|^2}\right)e^{-|\mathbf{k}_{\mathbf{J}}|^2/4E^2}e^{-j\,\mathbf{u}\cdot\mathbf{k}_{\mathbf{J}}} + \sum_{\mathbf{I}}\frac{1}{4\pi}\left(-\frac{e^{-(E\rho_{\mathbf{I}})^2}}{2E\sqrt{\pi}} + \frac{1}{2}\rho_{\mathbf{I}}\big(1 - \operatorname{erf}(E\rho_{\mathbf{I}})\big)\right)e^{-j\mathbf{k}\cdot\mathbf{r}_{\mathbf{I}}}. \tag{A8}$$

The mixed representation has a Gaussian convergence rate irrespective of the relative position of the observation point in the unit cell. As before, an appropriate choice for the $E$ parameter is $E = \sqrt{\pi}/V_{\text{cell}}^{1/3}$.

## Appendix B

Here, we prove the equivalence between the original eigensystem (1) and the integral-differential eigensystem (2).

To begin with, we prove that the mapping $\mathbf{E} \to (\tilde{\mathbf{E}}, \mathbf{f})$, defined by (5) and (6), transforms solutions of (1) into solutions of (2). Let $\mathbf{E}$ represent a generic electromagnetic mode, i.e., a solution of (1). The auxiliary field $\tilde{\mathbf{E}}$ defined by (6) is continuous over all space. Indeed, the second term on the right-hand side of (6) is continuous because the vector potential has the same regularity properties as in the free-space case [19, p. 59]. Similarly, the third term is also continuous because the singularity of $\nabla G_1$ for $\mathbf{r} = \mathbf{r}'$ is not as severe as that of $\Phi_p$. On the other hand, the first term is clearly discontinuous because the normal component of the electric field is discontinuous over the metallic interfaces. Let $[\mathbf{E}] = \mathbf{E}_+ - \mathbf{E}_-$, where $\mathbf{E}_+$ and $\mathbf{E}_-$ represent the electric field calculated from the outer side and from the inner side of $\partial D$, respectively. Since the tangential component of the electric field is continuous, we have that the "jump discontinuity" at $\partial D$ is $[\mathbf{E}] = ([\mathbf{E}]\cdot\hat{\boldsymbol{\nu}})\hat{\boldsymbol{\nu}}$. Finally, the fourth term in (6) is also discontinuous because it has the same jump discontinuity as the single layer potential in the free-space case [19, p. 51]. We then have

$$\left[\nabla\int_{\partial D}\nabla'_S\cdot\mathbf{f}\Phi_p(\mathbf{r}\,|\,\mathbf{r}')ds'\right] = -\nabla_S\cdot\mathbf{f}\,\hat{\boldsymbol{\nu}}, \qquad \mathbf{r}\in\partial D \tag{B1}$$

where the rectangular brackets represent as before the jump discontinuity of a vector field over the metallic interface, i.e., refer to the vector inside brackets calculated from the outer side of $\partial D$ minus the vector calculated from the inner side of $\partial D$. However, from (5), we have

$$\begin{aligned}\nabla_S\cdot\mathbf{f} &= j\beta Z_0\nabla_S\cdot\big(\hat{\boldsymbol{\nu}}\times[\mathbf{H}]\big)\\ &= -j\beta Z_0\hat{\boldsymbol{\nu}}\cdot\nabla\times[\mathbf{H}]\\ &= \beta^2\hat{\boldsymbol{\nu}}\cdot[\mathbf{E}], \qquad \mathbf{r}\in\partial D.\end{aligned} \tag{B2}$$

Hence, we conclude that the discontinuities of the first and fourth parcels in (6) cancel out and the auxiliary field $\tilde{\mathbf{E}}$ is indeed continuous.

Equation (3) implies that $\nabla^2\Phi_p = 0$ for $\mathbf{r}\notin\partial D_{\mathbf{I}}$ and $\mathbf{r}'\in\partial D$. Thus, from (6) and using (1) and (4), we find that for $\mathbf{r}\notin\partial D_{\mathbf{I}}$ (i.e., off the metallic interfaces)

$$\nabla\times\tilde{\mathbf{E}} = -j\beta Z_0\mathbf{H} + \nabla\times\int_{\partial D}\mathbf{f}(\mathbf{r}')\Phi_p(\mathbf{r}\,|\,\mathbf{r}')ds' \tag{B3a}$$

$$\nabla\cdot\tilde{\mathbf{E}} = 0. \tag{B3b}$$

To obtain (B3b), we used the identity (note that $\Phi_p(\mathbf{r}\,|\,\mathbf{r}') = \Phi_p(\mathbf{r}-\mathbf{r}')$) [19, p. 61]

$$\nabla\cdot\int_{\partial D}\mathbf{f}(\mathbf{r}')\Phi_p(\mathbf{r}\,|\,\mathbf{r}')ds' = \int_{\partial D}\nabla'_S\cdot\mathbf{f}\Phi_p(\mathbf{r}\,|\,\mathbf{r}')ds'. \tag{B4}$$

Since $\tilde{\mathbf{E}}$ is continuous, (B3) holds in the distributional sense over all space (note that, if $\tilde{\mathbf{E}}$ were discontinuous, delta-function distributions would arise for $\mathbf{r}\in\partial D_{\mathbf{I}}$). We also note that the right-hand side of (B3a) is continuous over all space. Indeed, its jump discontinuity is given by

$$\left[-j\beta Z_0\mathbf{H} + \nabla\times\int_{\partial D}\mathbf{f}(\mathbf{r}')\Phi_p(\mathbf{r}\,|\,\mathbf{r}')\,ds'\right] = -j\,\beta Z_0[\mathbf{H}] - \hat{\boldsymbol{\nu}}\times\mathbf{f}, \qquad \mathbf{r}\in\partial D \tag{B5}$$

where $\hat{\boldsymbol{\nu}}$ is the outward unit vector normal to $\partial D$ and the rectangular brackets stand for the jump discontinuity at the metallic interface. To obtain the above result, we used the fact that the vector potential has the same regularity properties as in the free-space case [19, p. 59]. Thus, its curl satisfies the jump relation

$$\left[\nabla\times\int_{\partial D}\mathbf{f}(\mathbf{r}')\Phi_p(\mathbf{r}\,|\,\mathbf{r}')ds'\right] = -\hat{\boldsymbol{\nu}}\times\mathbf{f}, \qquad \mathbf{r}\in\partial D. \tag{B6}$$

Since $\hat{\boldsymbol{\nu}}\cdot[\mathbf{H}] = 0$ (i.e., the normal component of the magnetic field is continuous), it follows from (5) that the right-hand side

of (B5) vanishes and that $\nabla \times \tilde{\mathbf{E}}$ can be extended to all space as continuous vector field.

From (B3), and using (1), (3), and the vector identity $\nabla \times \nabla \times = \nabla\nabla \cdot - \nabla^2$, we obtain

$$\nabla^2 \tilde{\mathbf{E}} = -\beta^2 \mathbf{E} - \nabla\nabla \cdot \int_{\partial D} \mathbf{f}(\mathbf{r}') \Phi_p(\mathbf{r} \,|\, \mathbf{r}')\, ds', \qquad \mathbf{r} \notin \partial D_{\mathbf{I}}. \tag{B7}$$

Using (B4), the previous equation can be rewritten as

$$\nabla^2 \tilde{\mathbf{E}} = -\beta^2 \mathbf{E} - \nabla \int_{\partial D} \nabla'_S \cdot \mathbf{f} \Phi_p(\mathbf{r} \,|\, \mathbf{r}')\, ds'. \tag{B8}$$

Since $\nabla \times \tilde{\mathbf{E}}$ and $\nabla \cdot \tilde{\mathbf{E}}$ can be extended continuously to all space (as has been proven before), the above formula is valid in the distributional sense over all space. Using arguments analogous to those employed before it can also be verified that the right-hand side of (B8) is continuous over all space. Thus, the vector field $\tilde{\mathbf{E}}$ and its derivatives are necessarily continuous up to order two (inclusive) over all space (including on the metallic interfaces). Moreover, using (6), it follows that $(\tilde{\mathbf{E}}, \mathbf{f})$ indeed verifies (2a). In what follows, we prove that $(\tilde{\mathbf{E}}, \mathbf{f})$ also verifies (2c) and thus that the mapping $\mathbf{E} \to (\tilde{\mathbf{E}}, \mathbf{f})$ indeed transforms solutions of (1) into solutions of (2).

We note that from (1c) the tangential component of the electric field vanishes on the metallic interfaces. Thus, using (6), we obtain

$$\begin{aligned} &\mathbf{w}^*(\mathbf{r}) \cdot \tilde{\mathbf{E}}(\mathbf{r}) - \mathbf{w}^*(\mathbf{r}) \cdot \int_{\partial D} \mathbf{f}(\mathbf{r}') \Phi_p(\mathbf{r} \,|\, \mathbf{r}') ds' \\ &\quad + \mathbf{w}^*(\mathbf{r}) \cdot \nabla \int_{\partial D} \nabla'_S \cdot \mathbf{f} G_1(\mathbf{r} \,|\, \mathbf{r}')\, ds' \\ &\quad = \frac{1}{\beta^2} \mathbf{w}^*(\mathbf{r}) \cdot \nabla \int_{\partial D} \nabla'_S \cdot \mathbf{f} \Phi_p(\mathbf{r} \,|\, \mathbf{r}')\, ds', \qquad \mathbf{r} \in \partial D \end{aligned} \tag{B9}$$

where $\mathbf{w} = \mathbf{w}(\mathbf{r})$ is an arbitrary tangential density defined on $\partial D$. Next we integrate (over the $\mathbf{r}$ coordinates) both sides of the equation over $\partial D$. Using standard vector identities, we readily obtain (2c). Thus, we have proven that the mapping $\mathbf{E} \to (\tilde{\mathbf{E}}, \mathbf{f})$ transforms solutions of (1) into solutions of (2).

Reciprocally, it is easy to verify that the mapping $(\tilde{\mathbf{E}}, \mathbf{f}) \to \mathbf{E}$ obtained from (6) transforms solutions of (2) into solutions of (1). Indeed, (1c) is equivalent to (2c), whereas (1a) and (1b) are equivalent to

$$\nabla^2 \mathbf{E} + \beta^2 \mathbf{E} = 0 \quad \nabla \cdot \mathbf{E} = 0, \qquad \mathbf{r} \notin \partial D_{\mathbf{I}} \tag{B10}$$

which readily follow from (2) and (6).

It can also be verified that the mapping $\mathbf{E} \to (\tilde{\mathbf{E}}, \mathbf{f})$ is indeed the inverse of $(\tilde{\mathbf{E}}, \mathbf{f}) \to \mathbf{E}$ and, thus, the proof is concluded.

## APPENDIX C

Here, we study some properties of the sesquilinear forms defined by (19) and (20). To begin with, we note that due to (A1) and (A3) we have that $\Phi_p(\mathbf{r} \,|\, \mathbf{r}') = \Phi_p^*(\mathbf{r}' \,|\, \mathbf{r})$ and $G_1(\mathbf{r} \,|\, \mathbf{r}') = G_1^*(\mathbf{r}' \,|\, \mathbf{r})$. This implies that the forms have Hermitian symmetry as follows:

$$\langle \mathbf{h}_1 \,|\, \mathbf{h}_2 \rangle_{\partial D, \Phi, G_1} = \langle \mathbf{h}_2 \,|\, \mathbf{h}_1 \rangle^*_{\partial D, \Phi, G_1} \tag{C1a}$$

$$\langle h_1 \,|\, h_2 \rangle_{\partial D, \Phi} = \langle h_2 \,|\, h_1 \rangle^*_{\partial D, \Phi}. \tag{C1b}$$

The form $\langle\, | \,\rangle_{\partial D, \Phi}$ is positive definite, i.e., $\langle h \,|\, h \rangle_{\partial D, \Phi} > 0$ if $h \neq 0$. In fact, from (20) and (A1), we have

$$\begin{aligned} \langle h \,|\, h \rangle_{\partial D, \Phi} &= \int_{\partial D} \int_{\partial D} h^*(\mathbf{r}) h(\mathbf{r}') \frac{1}{V_{\text{cell}}} \sum_{\mathbf{J}} \frac{e^{-j\mathbf{k_J} \cdot (\mathbf{r} - \mathbf{r}')}}{|\mathbf{k_J}|^2}\, ds' ds \\ &= \frac{1}{V_{\text{cell}}} \sum_{\mathbf{J}} \frac{1}{|\mathbf{k_J}|^2} \left| \int_{\partial D} h(\mathbf{r}') e^{j\mathbf{k_J} \cdot \mathbf{r}'}\, ds' \right|^2. \end{aligned} \tag{C2}$$

Since the form $\langle\, | \,\rangle_{\partial D, \Phi}$ is positive definite, we also conclude that it defines a scalar product over $\partial D$.

## REFERENCES


[1] K. Sakoda, *Optical Properties of Photonic Crystals*, ser. Opt. Sci. Berlin, Germany: Springer, 2001, vol. 80.

[2] E. Yablonovitch, "Inhibited spontaneous emission in solid-state physics and electronics," *Phys. Rev. Lett.*, vol. 58, pp. 2059–2062, May 1987.

[3] A. S. Barlevy and Y. Rahmat-Samii, "Characterization of electromagnetic band-gaps composed of multiple periodic tripods with interconnecting vias: Concept analysis, and design," *IEEE Trans. Antennas Propagat.*, vol. 49, pp. 343–353, Mar. 2001.

[4] D. R. Smith, W. J. Padilla, D. C. Vier, S. C. Nemat-Nasser, and S. Schultz, "Composite medium with simultaneously negative permeability and permittivity," *Phys. Rev. Lett.*, vol. 84, pp. 4184–4187, May 2000.

[5] M. Thevenot, C. Cheype, A. Reineix, and B. Jecko, "Directive photonic-bandgap antennas," *IEEE Trans. Microwave Theory Tech.*, vol. 47, pp. 2115–2122, Nov. 1999.

[6] C. Kyriazidou, H. F. Contopanagos, and N. Alexópoulos, "Monolithic waveguide filters using printed photonic-bandgap materials," *IEEE Trans. Microwave Theory Tech.*, vol. 49, pp. 297–307, Feb. 2001.

[7] C. T. Chan, Q. L. Yu, and K. M. Ho, "Order-$N$ spectral method for electromagnetic waves," *Phys. Rev. B, Condens. Matter*, vol. 51, pp. 16 635–16642, 1995.

[8] J. B. Pendry and A. MacKinnon, "Calculation of photon dispersion relations," *Phys. Rev. Lett.*, vol. 69, pp. 2772–2775, 1992.

[9] M. Silveirinha and C. A. Fernandes, "Efficient calculation of the band structure of artificial materials with cylindrical metallic inclusions," *IEEE Trans. Microwave Theory Tech.*, vol. 51, pp. 1460–1466, May 2003.

[10] ——, "A hybrid method for the calculation of the band structure of 2D photonic crystals," in *Proc. IEEE APS/URSI Symp.*, vol. 4, San Antonio, TX, June 2002, pp. 348–351.

[11] H. S. Sozuer, J. W. Haus, and R. Inguva, "Photonic bands: Convergence problems with the plane-wave method," *Phys. Rev. B, Condens. Matter*, vol. 45, pp. 13 962–13 972, June 1992.

[12] P. R. Villeneuve and M. Piché, "Photonic bandgaps: What is the best numerical representation of periodic structures?," *J. Mod. Opt.*, vol. 41, pp. 241–256, 1994.

[13] R. D. Meade, A. M. Rappe, K. D. Brommer, J. D. Joannopoulos, and O. L. Alerhand, "Accurate theoretical analysis of photonic band-gap materials," *Phys. Rev. B, Condens. Matter*, vol. 48, pp. 8434–8437, Sept. 1993.

[14] G. Conciauro, M. Bressan, and C. Zuffada, "Waveguide modes via an integral equation leading to a linear matrix eigenvalue problem," *IEEE Trans. Microwave Theory Tech.*, vol. MTT-32, pp. 1495–1504, Nov. 1984.

[15] P. Arcioni, M. Bressan, and L. Perregrini, "A new boundary integral approach to the determination of the resonant modes of arbitrarily shapes cavities," *IEEE Trans. Microwave Theory Tech.*, vol. 43, pp. 1848–1856, Aug. 1995.

[16] M. Silveirinha and C. A. Fernandes, "A new method with exponential convergence to evaluate the periodic Green's function," in *Proc. IEEE APS/URSI Symp.*, vol. 2, Columbus, OH, June 2003, pp. 805–808.

[17] P. P. Ewald, "Die berechnung optischer und elektrostatischer gitterpotentiale," *Ann. Der Phys.*, vol. 64, pp. 253–287, 1921.

[18] M. Silveirinha, "Electromagnetic Waves in Artificial Media with Application to Lens Antennas," Ph.D. dissertation, Dept. Elect. Comput. Eng., Univ. Técnica de Lisboa, Lisbon, Portugal, 2003.
[19] D. Colton and R. Kress, *Integral Equation Methods in Scattering Theory*. New York: Wiley, 1983.
[20] W. H. Press, *Numerical Recipes in C: The Art of Scientific Computing*. Cambridge, U.K.: Cambridge Univ. Press, 1988–1992.
[21] W. Y. Zhang, X. Y. Lei, Z. L. Wang, D. G. Zheng, W. Y. Tam, C. T. Chan, and P. Sheng, "Robust photonic band gap from tunable scatterers," *Phys. Rev. Lett.*, vol. 84, pp. 2853–2856, 2000.
[22] R. E. Collin, *Field Theory of Guided Waves*, 2nd ed. New York: IEEE Press, 1991.
[23] J. L. Blanchard, E. H. Newman, and M. Peters, "Integral equation analysis of artificial media," *IEEE Trans. Antennas Propagat.*, vol. 42, pp. 727–731, May 1994.
[24] C. A. Moses and N. Engheta, "Electromagnetic wave propagation in the wire medium: A complex medium with long thin inclusions," *Wave Motion*, vol. 34, pp. 301–317, 2001.
[25] S. Datta, C. T. Chan, K. M. Ho, and C. M. Soukoulis, "Effective dielectric constant of periodic composite structures," *Phys. Rev. B, Condens. Matter*, vol. 48, pp. 14 936–14 943, 1993.
[26] M. Silveirinha and C. A. Fernandes, "Effective permittivity of metallic crystals: A periodic Green's function formulation," *Electromagnetics*, vol. 23, no. 8, pp. 647–663, 2003.
[27] D. F. Sievenpiper, M. E. Sickmiller, and E. Yablanovitch, "3D wire mesh photonic crystals," *Phys. Rev. Lett.*, vol. 76, pp. 2480–2483, 1996.
[28] P. A. Belov, R. Marqués, S. I. Maslovski, I. S. Nefedov, M. Silveirinha, C. R. Simovsky, and S. A. Tretyakov, "Strong spatial dispersion in wire media in the very large wavelength limit," *Phys. Rev. B, Condens. Matter*, vol. 67, 1–4, 2003. 113 103.
[29] V. G. Veselago, "Electrodynamics of substances with simultaneously negative electrical and magnetic permeabilities," *Sov. Phys.—Usp.*, vol. 10, pp. 509–514, 1968.
[30] R. Marqués, F. Medina, and R. Rafii-El-Idrissi, "Role of bianisotropy in negative permeability and left-handed materials," *Phys. Rev. B, Condens. Matter*, vol. 65, pp. 144 440(1)–144 440(6), 2002.

**Mário G. Silveirinha** (S'99–M'03) received the Licenciado degree in electrical engineering from the University of Coimbra, Coimbra, Portugal, in 1998, and the Ph.D. degree in electrical and computer engineering from the Instituto Superior Técnico (IST), Technical University of Lisbon, Lisbon, Portugal, in 2003.

His research interests include propagation in photonic crystals and homogenization and modeling of metamaterials.

**Carlos A. Fernandes** (S'86–M'89) received the Licenciado, M.Sc., and Ph.D. degrees in electrical and computer engineering from the Instituto Superior Técnico (IST), Technical University of Lisbon, Lisbon, Portugal, in 1980, 1985, and 1990, respectively.

In 1980, he joined the IST, where, since 1993, he has been an Associate Professor with the Department of Electrical and Computer Engineering in the areas of microwaves, radio-wave propagation, and antennas. Since 1993, he has also been a Senior Researcher with the Instituto de Telecomunicações, where he is currently the Coordinator of the wireless communications scientific area. He has been the leader of antenna activity in national and European projects such as RACE 2067–MBS (Mobile Broadband System), and ACTS AC230–SAMBA (System for Advanced Mobile Broadband Applications). He has coauthored a book, a book chapter, and several technical papers in international journals and conference proceedings in the areas of antennas and radio-wave propagation modeling. His current research interests include artificial dielectrics, dielectric antennas for millimeter-wave applications, and propagation modeling for mobile communication systems.